



Direct Measurements of Synchrotron-emitting Electrons at Near-Sun Shocks

I. C. Jebaraj¹, O. V. Agapitov^{2,3}, M. Gedalin⁴, L. Vuorinen^{1,5}, M. Miceli⁶, C. M. S. Cohen⁷, A. Voshchepynets^{2,8}, A. Kouloumvakos⁹, N. Dresing¹, A. Marmyleva¹⁰, V. Krasnoselskikh^{2,11}, M. Balikhin¹², J. G. Mitchell¹³, A. W. Labrador¹³, N. Wijsen¹⁴, E. Palmerio¹⁵, L. Colombari², J. Pomoell¹⁰, E. K. J. Kilpua¹⁰, M. Pulupa², F. S. Mozer², N. E. Raouafi⁹, D. J. McComas¹⁶, S. D. Bale^{2,17}, and R. Vainio¹

¹Department of Physics and Astronomy, University of Turku, 20500 Turku, Finland; immanuel.c.jebaraj@gmail.com

²Space Sciences Laboratory, University of California, Berkeley, CA 94720, USA

³Astronomy and Space Physics Department, National Taras Shevchenko University of Kyiv, 03127 Kyiv, Ukraine

⁴Department of Physics, Ben Gurion University of the Negev, Beer-Sheva 84105, Israel

⁵Department of Physics and Astronomy, Queen Mary University of London, London E1 4NS, UK

⁶Dipartimento di Fisica e Chimica E. Segrè, Università degli Studi di Palermo, Palermo, 90134, Italy

⁷California Institute of Technology, Pasadena, CA 91125, USA

⁸Department of System Analysis and Optimization Theory, Uzhhorod National University, 88000 Uzhhorod, Ukraine

⁹The Johns Hopkins University Applied Physics Laboratory, Laurel, MD 20723, USA

¹⁰University of Helsinki, 00014 Helsinki, Finland

¹¹LPC2E/CNRS, UMR 7328, 45071 Orléans, France

¹²University of Sheffield, Sheffield S10 2TN, UK

¹³Heliophysics Science Division, NASA Goddard Space Flight Center, Greenbelt, MD 20771, USA

¹⁴Centre for Mathematical Plasma Astrophysics, KU Leuven, 3001 Leuven, Belgium

¹⁵Predictive Science Inc., San Diego, CA 92121, USA

¹⁶Department of Astrophysical Sciences, Princeton University, Princeton, NJ 08544, USA

¹⁷Physics Department, University of California, Berkeley, CA 94720, USA

Received 2024 September 16; revised 2024 October 18; accepted 2024 November 2; published 2024 November 14

Abstract

In this study, we present the first-ever direct measurements of synchrotron-emitting heliospheric traveling shocks, intercepted by the Parker Solar Probe (PSP) during its close encounters. Given that much of our understanding of powerful astrophysical shocks is derived from synchrotron radiation, these observations by PSP provide an unprecedented opportunity to explore how shocks accelerate relativistic electrons and the conditions under which they emit radiation. The probe's unparalleled capabilities to measure both electromagnetic fields and energetic particles with high precision in the near-Sun environment has allowed us to directly correlate the distribution of relativistic electrons with the resulting photon emissions. Our findings reveal that strong quasi-parallel shocks emit radiation at significantly higher intensities than quasi-perpendicular shocks due to the efficient acceleration of ultrarelativistic electrons. These experimental results are consistent with theory and recent observations of supernova remnant shocks and advance our understanding of shock physics across diverse space environments.

Unified Astronomy Thesaurus concepts: [Interplanetary shocks \(829\)](#); [Shocks \(2086\)](#); [Non-thermal radiation sources \(1119\)](#); [Solar radio emission \(1522\)](#); [Radio continuum emission \(1340\)](#); [Radio sources \(1358\)](#); [Solar coronal mass ejection shocks \(1997\)](#); [Solar particle emission \(1517\)](#)

1. Introduction

Collisionless shocks are among the most ubiquitous and strongly nonlinear systems in plasma, spanning spatial scales from laboratory settings to galaxy clusters (R. Z. Sagdeev 1966; A. A. Galeev 1976; C. F. Kennel et al. 1985; B. Lembège et al. 2004; V. Krasnoselskikh et al. 2013; O. V. Agapitov et al. 2023; M. Miceli 2023). In the shock reference frame, most of the directed flow's kinetic energy is converted into plasma heating, particle acceleration, magnetic compression, and turbulence. Understanding the mechanisms behind this energy conversion presents a significant challenge. Electron heating and acceleration to relativistic energies are key channels of energy redistribution, and the analysis of the electromagnetic (EM) radiation from these electrons is crucial for remote study of astrophysical shocks (J. Vink 2020).

Of particular interest is synchrotron radiation emitted by relativistic electrons accelerated at shock waves (J. Schwininger 1949; M. Born & E. Wolf 1964; V. L. Ginzburg & S. I. Syrovatskii 1964), which is the most common EM emission observed from supernova remnant (SNR) shocks (A. M. Bykov 2004; E. A. Helder et al. 2009), spanning from radio to X-ray wavelengths. The energy of these electrons is given by $E_e = \gamma m_e c^2$, where $\gamma (\gg 1)$ is the Lorentz factor, m_e is the electron mass, and c is the speed of light. Consequently, synchrotron emission is highly beamed within an angle $\theta \sim 1/\gamma$ around the electron's velocity direction. The emission power peaks at the critical frequency, $\omega_m \sim \Omega_e \gamma^2$, where $\Omega_e = eB/m_e c$ is the nonrelativistic electron gyrofrequency, with e being the electron charge and B the ambient magnetic field (V. L. Ginzburg 1979; M. S. Longair 1992). The synchrotron spectrum is broadband, with a width $\Delta\omega \sim \omega_m$, and the total emitted power scales as $\mathcal{P} \sim \gamma^2$. However, this emission typically arises from a distribution of electrons, often following a power law with an exponent δ .

The acceleration of such power-law distributed electrons, which emit broadband radiation, is often described by the

diffusive shock acceleration (DSA) theory (W. I. Axford et al. 1977; G. F. Krymskii 1977; A. R. Bell 1978; R. D. Blandford & J. P. Ostriker 1978). In the strong shock limit (gas compression ratio, $r_{\text{gas}}=4$), DSA predicts a power-law electron energy distribution with $\delta = (r_{\text{gas}} + 2)/(r_{\text{gas}} - 1) = 2$ (M. A. Malkov & L. O. Drury 2001; A. M. Bykov et al. 2019). A typical synchrotron spectrum produced by such an electron distribution has two main features: a low-frequency turnover (ω_c) separating optically thick and thin regimes (V. L. Ginzburg & S. I. Syrovatskii 1964; G. B. Rybicki & A. P. Lightman 1979) and a high-frequency exponential cutoff due to the maximum electron energy, $\omega_{\text{max}} \sim \Omega_e \gamma_{\text{max}}^2$, where γ_{max} is the highest Lorentz factor in the distribution.

In the optically thin regime, the synchrotron spectrum follows a power law with an exponent $\alpha \sim 0.5$, which directly relates to the electron energy distribution ($\delta=2$) via $\alpha = (\delta - 1)/2$. This relationship is traditionally used to estimate particle distributions in astrophysical sources such as SNRs, though variations are common (D. A. Green 2019). Despite these insights, uncertainties remain about the detailed distribution of relativistic electrons, their acceleration mechanisms, and the specific conditions under which they emit radiation. The universality of DSA theory, particularly its scale invariance in strong shocks ($r_{\text{gas}}=4$), suggests that understanding synchrotron radiation in interplanetary (IP) shocks could offer a bridge to understanding SNR shocks. Such a bridge between IP and SNR shocks has long been sought, with the heliosphere often considered a practical laboratory for studying remote astrophysical objects (C. F. Kennel et al. 1985; T. Terasawa 2003). Observations of SNR shocks offer unique insights into the analysis of global shock structure through high-resolution radio astronomy, which allows for probing different regions of a shock with GeV electrons along various lines of sight. However, certain factors must be considered, such as the vast difference in system size, with SNR shocks being more than 6 orders of magnitude larger, and their lifetime is much longer. Similarly, the energy they carry is at least 15 orders of magnitude greater than that of the most powerful IP shocks (J. Vink 2020). Furthermore, the nonstationarity of acceleration, e.g., in traveling IP shocks, may substantially affect the particle spectrum, making comparison with SNR shocks more difficult.

A combination of remote-sensing observations of synchrotron emission and in situ measurements of the emitting electrons can address key questions about the conditions that produce accelerated electrons capable of synchrotron radiation. This approach could help reconcile differences between strong IP and SNR shocks, where system size and the upstream ion bulk energy in the shock frame are the primary distinctions. Earlier studies suggested that heliospheric synchrotron emission is generated by energetic electrons trapped within the coronal mass ejections driving the shock, rather than by shock-accelerated electrons (T. S. Bastian 2007; S. Pohjolainen et al. 2013). However, more recent work has shown that traveling IP shocks can accelerate electrons to relativistic energies (I. C. Jebaraj et al. 2023a, 2024; N. Talebpour Sheshvan et al. 2023).

In this study, we present the first-ever direct observations of synchrotron-emitting relativistic ($\gamma \sim 2-6$ or $E_e \sim 1-3$ MeV) and ultrarelativistic ($\gamma > 10$ or $E_e > 5$ MeV) electrons produced by fast IP shocks observed by NASA’s Parker Solar Probe (PSP; N. J. Fox et al. 2016). We utilize continuous, high-

fidelity electric field measurements in the radio wavelengths from the Radio Frequency Spectrometer (RFS; M. Pulupa et al. 2017), part of the FIELDS instrument suite (S. D. Bale et al. 2016). These observations are compared with the electron distributions measured at the time of shock arrival by the Low and High Energetic Particle Instruments (EPI-Lo and EPI-Hi, respectively; M. E. Hill et al. 2017; M. E. Wiedenbeck et al. 2017), part of the Integrated Science Investigation of the Sun (IS \odot IS) suite (D. J. McComas et al. 2016). The first shock (S1) was quasi-perpendicular and detected during PSP’s 13th close approach to the Sun (Encounter 13) on 2022 September 5 at $15.1 R_{\odot}$ (O. M. Romeo et al. 2023; D. Trotta et al. 2024). The second shock (S2) was near-parallel and detected $49 R_{\odot}$ away during Encounter 15 on 2023 March 13 (I. C. Jebaraj et al. 2024). In the following sections, we present our observations of synchrotron emission, analyze the spectral characteristics and polarization, and examine the distribution of the emitting electrons.

2. Results from the Analysis

2.1. Diffuse and Self-absorbed Continuum-like Emission

Figures 1(A) and (B) display the dynamic radio spectra of electric field intensity from transverse EM waves, $E(f, t)^2$, where $f = \omega/2\pi$ (in Hz), recorded by the high (HFR; 19.2–1.6 MHz) and low (LFR; 1.6–0.001 MHz) frequency receivers of FIELDS/RFS on board PSP, both before and during the shock crossings on 2022 September 5 (S1) and 2023 March 13 (S2), respectively. The units of measurement are solar flux units ($1 \text{ sfu} = 10^{-22} \text{ W m}^{-2} \text{ Hz}^{-1}$), normalized to 1 au, assuming that the intensity decreases with distance (r) following r^{-2} . These EM waves, emitted by electrons at some distance from the spacecraft, propagate toward the observer at the speed of light, appearing as distinct maxima in the electric field intensity. The frequencies of these maxima change over time, and the rate of change, hereafter referred to as “drift,” reflects variations in plasma density and magnetic field gradients in the emission region. In regions with negative gradients in plasma density and magnetic field, both $\omega_{pe} (= \sqrt{(n_e e^2)/(4\pi\epsilon_0 m_e)})$, where n_e is electron density and ϵ_0 is the permittivity of free space) and Ω_e will show negative gradients. As a result, analyzing spectral drift rates and assuming a model for the emission mechanism, properties of the emitting electrons and the surrounding medium can be inferred. The electron plasma frequency at the observer’s location, $f_{pe} = \omega_{pe}/2\pi$, is annotated in both Figures 1(A) and (B). Below f_{pe} , EM waves become evanescent, resulting in a sharp emission cutoff regardless of where the emission originates.

Figures 1(A) and (B) also annotate common coherent emissions generated by plasma instabilities (S. A. Kaplan & V. N. Tsytovich 1969; A. A. Galeev & V. V. Krasnoselskikh 1979; K. Papadopoulos & H. P. Freund 1979; A. Voshchepynets et al. 2015). This includes type II bursts, produced by subrelativistic electrons accelerated at shocks. This emission is characterized by a narrow relative frequency bandwidth ($\Delta f/f = (f_{\text{high}} - f_{\text{low}})/f_{\text{center}} < 0.3$, where $f_{\text{center}} = (f_{\text{high}} + f_{\text{low}})/2$; I. H. Cairns et al. 2003; I. C. Jebaraj et al. 2020). In the spectra, type II bursts appear as chains of intense, fragmented emissions with frequency drift corresponding to the speed of the shock region where they originate. Additionally, type III bursts are generated by subrelativistic electron beams propagating along open magnetic field lines,

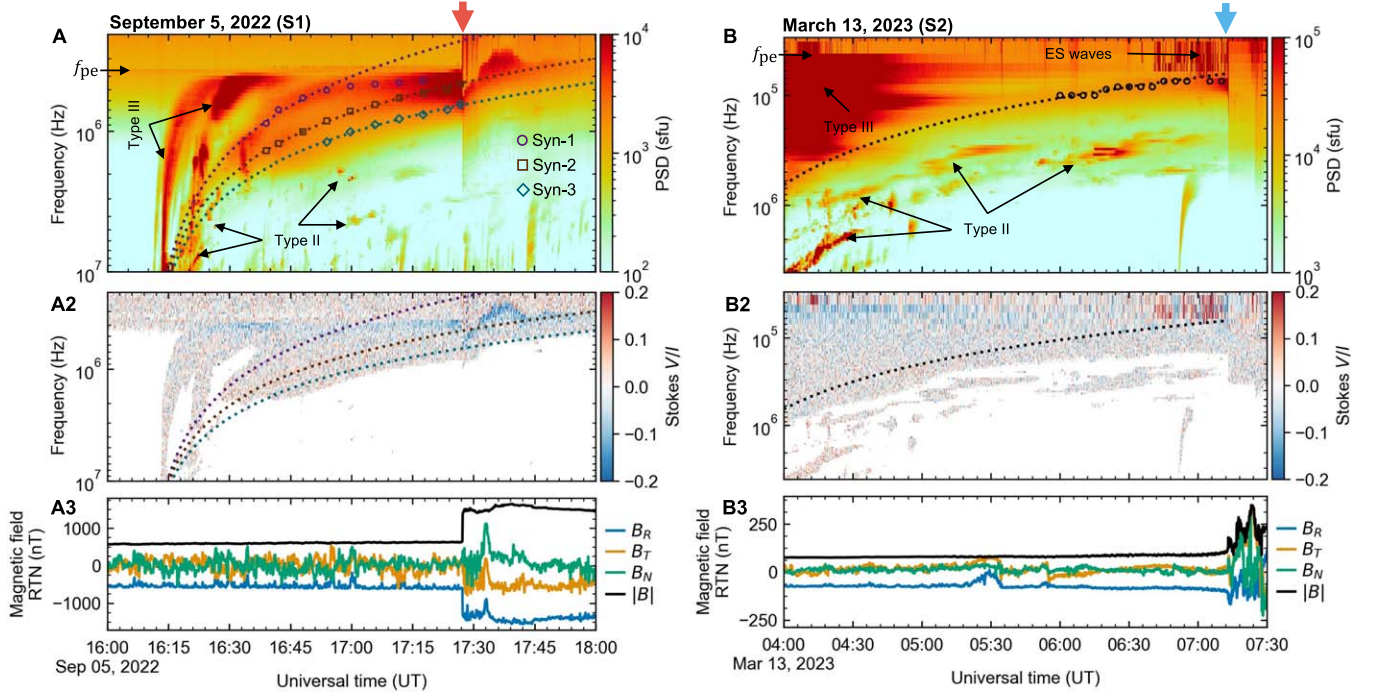


Figure 1. Panels (A) and (B) (top row) show the dynamic spectra of electric field power, $E(f, t)^2$, in the radio frequency range, measured before and at the shock crossing on 2022 September 5 (S1) and 2023 March 13 (S2), respectively. The units are in solar flux units ($1 \text{ sfu} = 10^{-22} \text{ W m}^{-2} \text{ Hz}^{-1}$). The arrival of both shocks at PSP is marked by the red (S1) and blue (S2) arrows on top of the figure. The synchrotron emissions, the coherent plasma emissions (type II and type III), and the local f_{pe} are marked. Panels (A2) and (B2) (middle row) show the degree of circular polarization normalized by total intensity (Stokes V/I ; see text for details). Panels (A3) and (B3) (bottom row) show the magnetic field components and magnitude.

with $\Delta f/f \lesssim 0.5$ (S. Suzuki & G. A. Dulk 1985; I. C. Jebaraj et al. 2023b). Type III bursts, the most intense heliospheric radio emissions, exhibit rapid spectral drift rates, reflecting the high speed of the emitting electrons. While these emissions and their relationship to solar transient shocks have been extensively studied over the past five decades, this study focuses on spectral features beyond these well-known emissions.

2022 September 5 (S1). In Figure 1(A), we identify three distinct emissions that deviate from the characteristics of the aforementioned coherent emissions, annotated as Syn-1, Syn-2, and Syn-3. Syn-1 (circle markers) starts at ~ 5 MHz at 16:20 UT and drifts down to the local $f_{pe} \sim 400$ kHz by 17:00 UT, with some parts observed until shock arrival at 17:27 UT. Syn-2 (square markers) begins at ~ 2 MHz at 16:30 UT and drifts down to f_{pe} during shock arrival at 17:27 UT. Syn-3 (diamond markers) starts at ~ 2 MHz at 16:50 UT and similarly drifts down to f_{pe} by 17:27 UT. These emissions are characterized as diffuse, broadband emissions with $\Delta f/f \sim 1$, and the associated maxima (annotated with distinct markers) correspond to the turnover frequency ($f_c = \omega_c/2\pi$). The features are indicative of synchrotron emission with self-absorption (A. Nindos 2020). It is worth noting that some emission is seen continuing in the postshock region up until 17:45 UT. Much of it is evanescent due to the high f_{pe} in the postshock plasma. Analysis in Appendix B shows that the measured electric field intensity corresponds to EM waves with phase speeds close to c , with no detection of Langmuir waves.

2023 March 13 (S2). In Figure 1(B), an emission starts at 05:20 UT from ~ 200 kHz and extends until shock arrival at 07:13 UT. This emission is also characterized as diffuse and broadband with $\Delta f/f \sim 1$, with f_c annotated with circle markers. A similar analysis of the EM waves near the shock arrival at 07:12 UT is presented in Appendix B. The estimated phase

speeds for the waves above f_{pe} were close to c . However, unlike S1, several electrostatic waves were detected at a small fraction of f_{pe} , annotated as “ES waves” in Figure 1(B). These waves are not expected to contribute to the generation of coherent plasma emissions (V. V. Lobzin et al. 2005).

2.2. Emission Is Depolarized in Inhomogeneous Plasma

Synchrotron radiation from a homogeneous medium is highly polarized (V. L. Ginzburg & S. I. Syrovatskii 1964). EM radiation is emitted as a combination of two transverse wave modes, distinguished by the orientation of the wave electric field (\mathbf{E}) relative to the background magnetic field (\mathbf{B}). These modes are the ordinary (o -mode, $\mathbf{E} \parallel \mathbf{B}$) and extraordinary (x -mode, $\mathbf{E} \perp \mathbf{B}$) waves. In a cold, unmagnetized plasma, the propagation of o - and x -modes is independent of each other, but this is not the case in a magnetoactive plasma. The transfer of these wave modes through a plasma is best described using the Stokes parameters: I , Q , U , and V (S. Chandrasekhar 1947; R. Ramaty 1969). A short description of the Stokes parameters and the means of estimating them from data can be found in Appendix D. When wave propagation is quasi-parallel to \mathbf{B} , the Stokes parameters simplify such that $Q = U \rightarrow 0$. As a result, o - and x -mode waves are circularly polarized in opposite directions, and Stokes V is given by the difference between the intensities of the o - and x -modes ($V = I_o - I_x$), resulting in circular polarization in the direction of the dominant mode. In the case of quasi-perpendicular wave propagation relative to \mathbf{B} , Stokes $Q = I_o - I_x$, while $U = V \rightarrow 0$, leading to predominantly linear polarization.

The polarization conventions described above apply strictly to the region where emission originates. If \mathbf{B} changes between the emitter and observer, the polarization can be altered or lost.

Stokes V may be converted to Stokes Q (and vice versa) due to Faraday conversion, potentially reducing or reversing the observed circular polarization (A. G. Sitenko & Y. A. Kirochkin 1966; V. V. Zheleznyakov 1968). Linear polarization can undergo Faraday rotation, where the polarization plane rotates during propagation, possibly leading to depolarization if the magnetic field is complex (A. G. Sitenko & Y. A. Kirochkin 1966; V. L. Ginzburg & S. I. Syrovatskii 1969; D. B. Melrose 1971). Precise measurement of polarization is impossible, as the waves may become depolarized while propagating through a plasma with random fluctuations. Consequently, for a remote observer, it may differ significantly from what it was at the region where it is emitted.

Synchrotron radiation is typically emitted over a range of angles with respect to \mathbf{B} , making the x -mode dominant for the observer. This also makes the emission linearly polarized in the x -mode when observed along the direction of the electron's velocity or from any oblique angles to \mathbf{B} . Thus, the degree of circular polarization is secondary and increases with $\theta \sim 1/\gamma$, or when viewed from oblique angles within θ . This can be reformulated in terms of Stokes parameters as $V/Q \sim 1/\gamma$. The handedness of circular polarization for the o -mode is strictly clockwise (right-handed) when the magnetic field is pointing inward ($B_r < 0$) and counterclockwise (left-handed) when it is pointing outward ($B_r > 0$). For the x -mode, the handedness is reversed.

The emissions from both S1 and S2 have negligible degrees of linear polarization and are not presented here. The degree of circular polarization ($(I_o - I_x)/(I_o + I_x) = V/I$) for both events is depicted in Figures 1(A2) and (B2).

2022 September 5 (S1). We observed clear circular polarization for Syn-2 and Syn-3 when the emission was close to the local f_{pe} during the shock arrival between 17:15 and 17:27 UT. Given that $V/Q \approx 1/\gamma$, we used the degree of circular polarization ($V/I = 15\% - 25\%$) to estimate that the emission originated from electrons with $\gamma \sim 4 - 7$. Figure 1(A3) shows the magnetic field components and magnitude, revealing that S1 is polarized in the left-hand sense, while $B_r < 0$ (inward-pointing), consistent with emission in the x -mode as predicted by theory. While remote observations can carry significant uncertainties when correlating with magnetic field data, our measurements were made with the emitting region in close proximity to the observer, thereby reducing much of this uncertainty.

2023 March 13 (S2). The observations presented in Figure 1(B2) show no signs of circular polarization. This lack of polarization is likely due to a combination of observer position and depolarization caused by a randomly inhomogeneous medium. If the conditions at and around the emitting region are turbulent at scales corresponding to the wavelength of the EM waves, they may be depolarized within the emitting region. Even in the presence of large-scale inhomogeneities, the Faraday effect may significantly depolarize the EM waves. Indeed, it was demonstrated by I. C. Jebaraj et al. (2024) that inhomogeneities across a wide range of scales were present.

2.3. Intrinsic Brightness Increases as Shock Approaches PSP

The characteristics of the synchrotron emission may also be assessed, taking into account the radiation transfer from the emitting electrons toward the observer (S. Chandrasekhar 1947). Under the Rayleigh–Jeans approximation ($hf \ll k_B T_B$, where h is Planck's constant, f is the frequency

of radiation in Hz, and k_B is the Boltzmann constant), $T_B \approx (c^2 I_f)/(2k_B f^2)$, where I_f is the emission intensity. The intrinsic brightness of the source or brightness temperature T_B of synchrotron emissions cannot exceed the limit set by inverse Compton scattering (10^{12} K at 1 GHz; K. I. Kellermann & I. I. K. Pauliny-Toth 1969; G. B. Rybicki & A. P. Lightman 1979). Quantifying the solid angle subtended by the source (Ω in units of steradians) allows us to estimate T_B (see Equation (C3) in Appendix C).

2022 September 5 (S1). In Figure 1(A), the maxima of Syn-1, Syn-2, and Syn-3 are annotated by the circle, square, and diamond markers, respectively. They correspond to the self-absorption cutoff or the f_c . If the source of the synchrotron emission is the relativistic electrons accelerated at the shock front that rapidly approaches the probe, then Ω increases at a rate determined by the shock speed. This suggests that the presence of different synchrotron emissions (Syn-1, Syn-2, and Syn-3) are likely due to different electron populations at different regions of the shock, which propagate at different speeds. Assessing Syn-2 and Syn-3, we find that their intensity increases with decreasing frequency, indicating a rapid increase in Ω , such that $\Omega \rightarrow 2\pi$.

The effect of Ω is such that as the region of the shock accelerating the electron gets closer and closer, emission from more and more electrons is received. Such an effect would also be seen in T_B , which was estimated for Syn-1, Syn-2, and Syn-3 in Appendix C. The result suggests that none of them exceed the inverse Compton scattering limit of 1.3×10^{13} K. However, the T_B of Syn-2 and Syn-3 increases rapidly just before the shock arrival at 17:27 UT, indicating that $\Omega \rightarrow 2\pi$, i.e., emission originates from regions in close proximity to the shock front traversed by the spacecraft. A schematic of the likely shock encounter is shown on the right in Figure 2, where the probe encounters the shock flank, which is quasi-perpendicular. The probe is positioned in close proximity to the emitting region (marked by the red square on the shock surface), allowing it to receive portions of the synchrotron radiation.

2023 March 13 (S2). Here, the intensity of the emission increases as the shock approaches. Quantifying this using the solid angle Ω , we find that T_B remains relatively stable until 06:55 UT, after which it increases exponentially as the shock nears the spacecraft, corresponding to $\Omega \rightarrow 2\pi$. Notably, T_B exceeds the inverse Compton limit of 1.7×10^{13} K, suggesting that $\Omega = 2\pi$ at 07:10 UT. This indicates that the spacecraft was inside the region where electron acceleration and subsequent emission were being generated. In this scenario, the observer receives emission from a source that covers the full 4π sr (i.e., a fully isotropic source), causing the 2π sr assumption to break down. The schematic on the left in Figure 2 illustrates the likely encounter between the probe and the shock wave. The probe encounters the center of the quasi-parallel shock region, where it receives the bulk of the emitted synchrotron photons, leading to a higher observed emission intensity. As noted in Figure 6 in Appendix C, the intrinsic brightness of the radiation from S2 is an order of magnitude greater than that of S1, supporting the representation shown in the schematic.

2.4. Relativistic Electron Distribution and the Optically Thin Synchrotron Spectra

The observations of synchrotron emission from shocks that traversed PSP provide a unique opportunity to directly probe

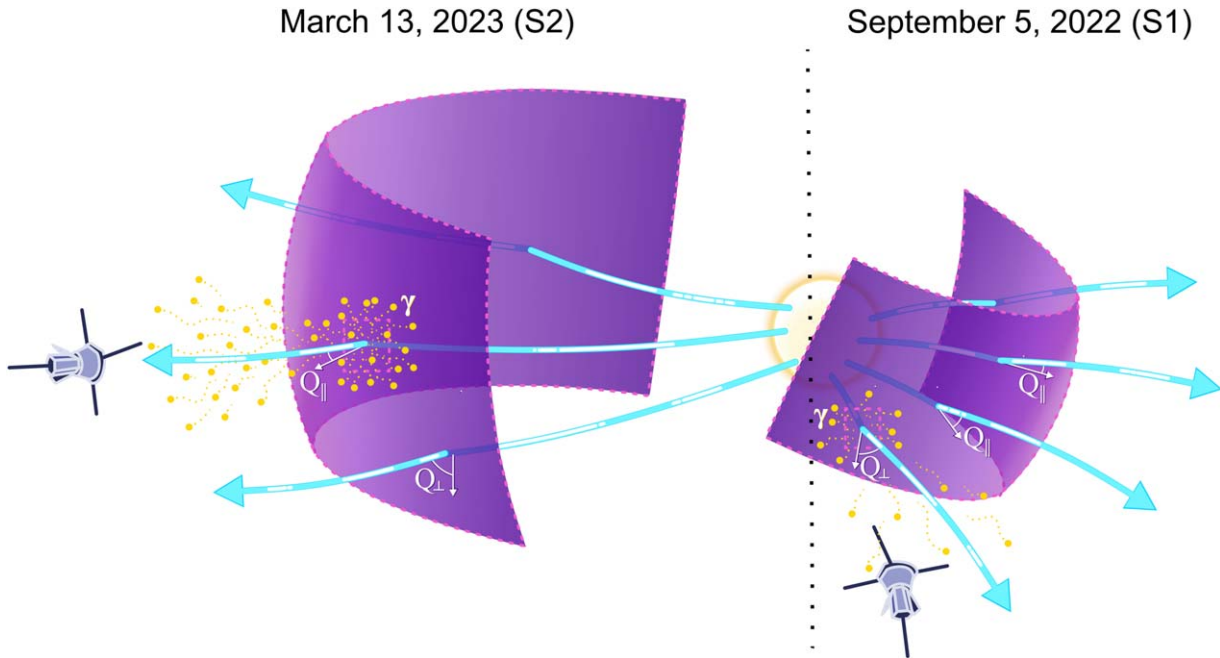


Figure 2. Schematic of the synchrotron emission from S1 and S2. The curved purple front represents the traveling shock wave, with magnetic field lines shown in blue. The shock geometry along the reference field lines is labeled as Q_{\perp} (quasi-perpendicular) and Q_{\parallel} (quasi-parallel). The finite region on the shock surface where relativistic electrons are accelerated and subsequently emit synchrotron radiation is indicated by the red square. The emitted photons are represented by yellow markers and the notation γ .

the energetic electron distribution and compare it with the synchrotron spectrum. This comparison may be approached from DSA theory, as the power-law exponents of the synchrotron spectrum (α) and that of the electrons (δ) are directly related through $\alpha \sim (\delta - 1)/2$.¹⁸ While the shock structure is relatively unimportant for high-energy ions undergoing DSA, it plays an important role for electron acceleration (M. A. Riquelme & A. Spitkovsky 2011). Furthermore, investigating the characteristics of the accelerated electrons such as their anisotropy may also improve our understanding of the process. In the presence of a well-developed ion foreshock, electrons scatter and their pitch angles become diffused, leading to an isotropic distribution (M. A. Malkov & L. O. Drury 2001).

If these shock characteristics play a significant role, we would expect to see differences between S1 and S2, given their distinct properties that have been discussed in O. M. Romeo et al. (2023) and I. C. Jebaraj et al. (2024). S1 was a fast shock that was propagating quasi-perpendicularly to the background \mathbf{B} and had moderate gas compression, $r_{\text{gas}} \sim 2.5$. S2 was also a fast shock but propagating nearly parallel to \mathbf{B} with maximum compression, $r_{\text{gas}} = 4$. While shock geometry is not a direct factor in DSA estimations, it plays a crucial role in creating the conditions that enable efficient particle acceleration via DSA, such as the development of a wave foreshock (L. O. Drury 1983; R. Vainio 2003). The formation of a foreshock is particularly effective in quasi-parallel shocks due to ion-streaming instabilities, which generate waves that act as scattering centers for both ions and relativistic electrons, thereby enhancing DSA (R. Vainio & R. Schlickeiser 1999). According to DSA theory, the predicted electron energy spectral index δ would be around 3 for S1 and closer to 2 for

S2, corresponding to synchrotron spectral slopes of $\alpha \sim 1$ for S1 and $\alpha = 0.5$ for S2. However, a limitation of DSA's applicability to electrons is that only those with $\gamma \gtrsim 2$ or $E_e \gtrsim 1$ MeV can participate effectively, as these electrons are able to interact with the waves generated by ions (G. P. Zank & T. K. Gaisser 1992; M. A. Malkov & L. O. Drury 2001). The technical requirement for electron involvement in DSA is less stringent than for their injection into it. The primary condition is that their speed must exceed that of the shock along the field line, which imposes additional constraints on DSA efficiency in quasi-perpendicular shocks, even in the presence of ion-scale waves.

While this study does not specifically address how and why subrelativistic electrons reach relativistic energies, the process remains poorly understood and presents a barrier to fully understanding electron acceleration. Previous studies have shown that electron energization is linked to the scale of the EM fields at the shock transition layer (M. Balikhin et al. 1993, 1998), which determines the contributions from both adiabatic and nonadiabatic processes (M. Gedalin 2020). In the case of S1, where the shock is quasi-perpendicular, much of the subrelativistic electron acceleration is likely to be adiabatic (M. A. Balikhin et al. 1989; I. C. Jebaraj et al. 2023b), although nonadiabatic processes may also play a role when the shock is supercritical (M. Gedalin et al. 1995; T. Katou & T. Amano 2019). In the case of S2, I. C. Jebaraj et al. (2024) found that the transition consisted of a series of large-amplitude quasi-perpendicular waves, with a wide range of electron-scale waves present in the foreshock. This combination makes it difficult to pinpoint a single mechanism, though adiabatic, nonadiabatic, and other diffusive mechanisms could coexist.

2022 September 5 (S1). To directly compare the accelerated electrons and the synchrotron radiation they emit, we fit the emission peaks f_c , marked with distinct indicators in

¹⁸ It is worth noting that for mildly relativistic electrons, G. A. Dulk & K. A. Marsh (1982) propose a modified form, $\alpha \sim 0.9\delta - 1.22$, resulting in a steeper spectrum.

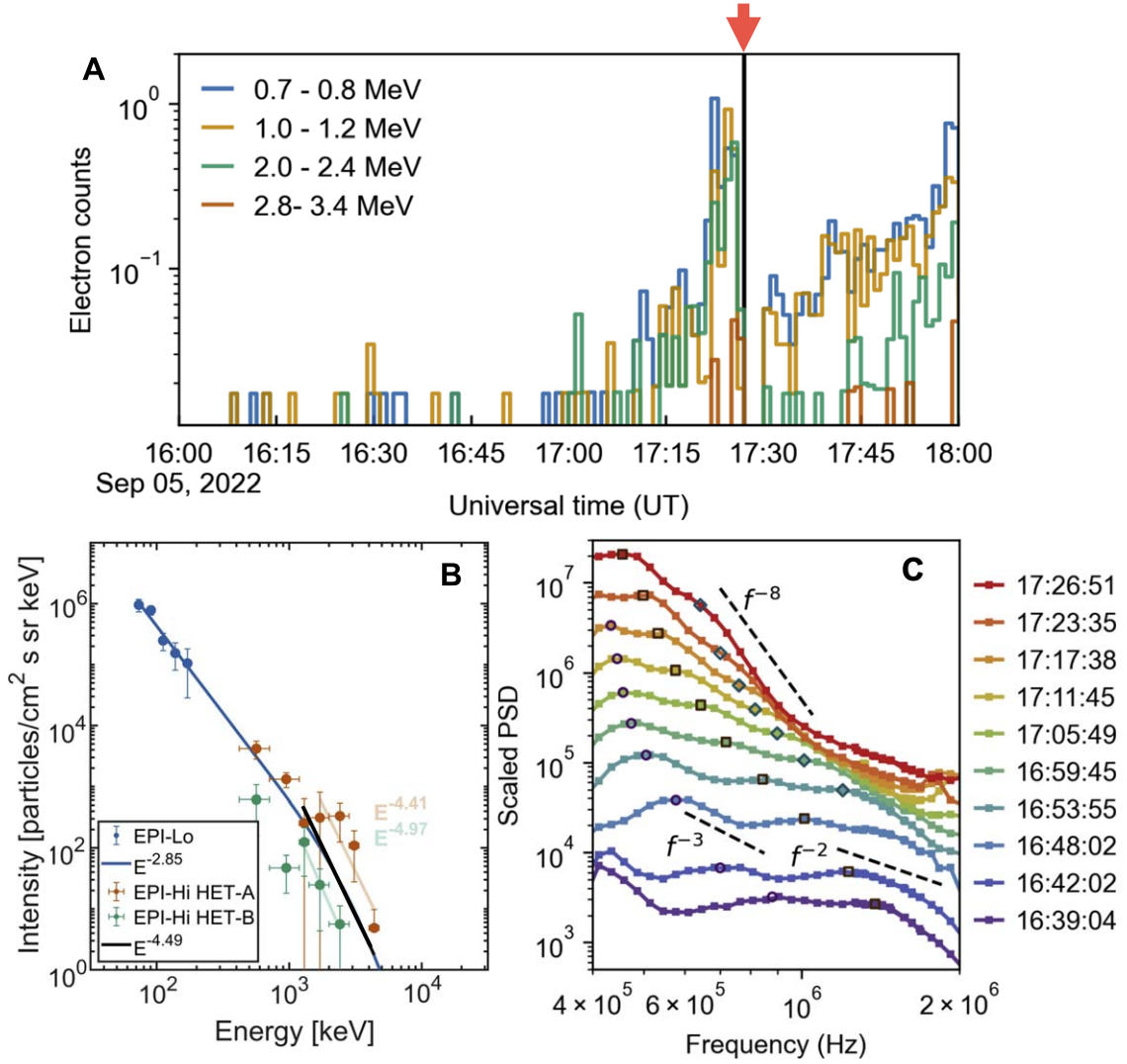


Figure 3. Characteristics of the synchrotron emission from S1 and the corresponding electron distribution. Panel (A) presents the time evolution of the electron intensity in units of counts s^{-1} observed between 16:00 UT and 18:00 UT. The arrival of the shock at PSP is marked by the vertical black line at 17:27 UT and the red arrow on top. Panel (B) shows the 10 minute averaged electron energy distribution between 17:17 and 17:27 UT in units of particles $cm^{-2} s^{-1} sr^{-1} keV^{-1}$. The different detectors of IS \odot IS used to construct the electron spectrum are annotated with colored markers. The approximate power-law fits and the exponents are also shown in the legend. Panel (C) shows the intensity–frequency profiles at specific times leading up to the shock arrival, along with approximate power-law fits and the exponents are also shown in the legend. The f_c for Syn-1, Syn-2, and Syn-3 are indicated by the distinct markers introduced in Figure 1(A).

Figure 1(A), using power laws. For the same time interval, we present the time evolution of the relativistic electron intensity (in unprocessed units of counts s^{-1}) measured by EPI-Hi High Energy Telescope (HET). The relativistic electron intensity rapidly increases approximately 5 minutes before the shock crossing and remains substantial and nearly constant up to the crossing itself. This suggests that relativistic electrons are found in a relatively small region upstream of the shock. In the postshock region, the relativistic electron intensity decreases significantly, suggesting that emission must be produced by electrons in the upstream. We construct the electron energy spectra shown in Figure 3(B) using data collected by the EPI-Lo and EPI-Hi/HET instruments during the shock crossing, between 17:17 and 17:27 UT. Both detectors of EPI-Hi/HET, namely, the Sun-facing HET-A and the anti-Sun-facing HET-B, are used. Unlike in Figure 3(A), the data used to construct the energy–intensity spectra are processed in units of intensity, i.e., particles $cm^{-2} s^{-1} sr^{-1} keV^{-1}$. We use a 10 minute average of the data to reduce large uncertainties that may arise

due to low statistics. Detailed information about the unfolding procedure used to construct the energy spectra and the associated errors is provided in Appendix A.2.

The energy spectra shown in Figure 3(B) span from subrelativistic energies, where $\gamma \sim 1$ or $E_e \sim 50$ keV, to 4 MeV (or $\gamma \sim 8$). Due to missing energy channels between 200 and 500 keV, we approximately fit a single power law from 50 keV up to 1 MeV, yielding an exponent $\delta \sim 2.85$. However, these electrons, with $\gamma \sim 1-2$, do not contribute significantly to synchrotron power, which scales as $\mathcal{P} \sim \gamma^2$. Beyond 1 MeV, uncertainties in HET measurements increase (see Appendix A.2), making precise determination of δ challenging. Despite these uncertainties, we observe a deviation from the power law obtained for lower energies beyond 1 MeV. A new power-law fit, combining data from HET-A and HET-B between 1 and 5 MeV, yields an exponent $\delta \sim 4.5$. However, when assessed separately, HET-A and HET-B do not follow the same trend and can be fit with separate power laws, with exponents $\delta \sim 4.4$ for HET-A (shown in red) and $\delta \sim 5$ for HET-B (shown in green).

Isolating the theoretically predicted shape of the synchrotron spectra is impossible in the presence of elevated background radiation from thermal and nonthermal sources during PSP's close encounters (M. Liu et al. 2023). Therefore, in what follows, we focus on identifying f_c as seen in Figure 1(A) and estimating α in the optically thin regime to infer the corresponding δ . Figure 3(C) shows temporal cuts of spectral power as a function of frequency at selected times between 16:42 UT and the shock arrival at 17:27 UT. We focus on Syn-2 (square markers) and Syn-3 (diamond markers), as Syn-1 (circle markers) reaches the local f_{pe} early and is not relevant to the locally measured electrons. For Syn-2 and Syn-3, f_c is well defined by intensity peaks, allowing for the estimation of the spectral slope α above f_c . Between 16:42 UT and 17:15 UT, we find $\alpha \sim 2$ ($\delta \sim 5$) for both Syn-2 and Syn-3, consistent with the $\delta \sim 4.5$ estimated from the in situ electron measurements (Figure 3(B)). After 17:15 UT, as f_c approaches f_{pe} , the minimum electron energy γ_{\min} required to emit above f_{pe} increases. In this case, emission originates from the steep tail of the electron distribution resulting in a steep $\alpha \gtrsim 8$ or $\delta \gtrsim 17$. Alternatively, this may be a result of the high-frequency exponential synchrotron cutoff, $f_{\max} = \omega_{\max}/2\pi$, at γ_{\max} of the electron distribution.

Interpreting these observations from a DSA perspective, we find that the power-law exponent of the low-energy electrons $\delta \sim 2.85$ aligns reasonably well with the prediction for S1, $\delta \sim 3$. However, DSA is not particularly effective for the acceleration of subrelativistic electrons, and it is likely that only electrons with energy $E_e \gtrsim 1$ MeV can efficiently participate in the process. The observations presented here show that at 1 MeV and above, the power-law exponent steepens to $\delta \sim 4.5$, suggesting that even if DSA is active, it is inefficient. The steepening of α also suggests that there is a cutoff in DSA close to $E_e \sim 4$ MeV. Here, we find varying electron intensities measured by HET-A and HET-B above $\gtrsim 1.5$ MeV. When the magnetic field is nominally oriented, the Sun (HET-A) and anti-Sun (HET-B) directions correspond to parallel (0°) and antiparallel (180°) pitch angles of the electrons. Since the electron intensity measured by HET-A is more than an order of magnitude higher than HET-B, it indicates strong anisotropy in the electrons observed from the Sun direction, where the shock is approaching the observer. Anisotropy is generally found when the accelerated particles do not partake in efficient DSA or in the absence of a well-developed foreshock.

2023 March 13 (S2). We present the temporal evolution of the relativistic electron population in Figure 4(A), which shows an increase in particle counts leading up to the shock arrival. Unlike in S1, the relativistic electron intensity in S2 is relatively high, with a noticeable increase starting at $\sim 06:40$ UT and continuing until the shock's arrival at 07:13 UT. Figure 4(B) illustrates the average electron energy-intensity spectrum in a 10 minute interval upstream of the shock arrival. Using a similar power-law fitting as for S1, we found an exponent of $\delta \sim 2.7$ between 50 keV and 2.5 MeV ($\gamma \sim 4$). Unlike S1, the power law extends beyond subrelativistic energies up to $\gamma \sim 4$, making it more relevant for synchrotron emission. Beyond ~ 2.5 MeV, the spectrum transitions into a much steeper power law or exhibits an exponential rollover. Despite increased uncertainties due to the instrument's dynamic threshold mode (see Appendix A.2), we approximate a power-law fit for these data and obtain an exponent of $\delta \sim 4.18$.

Next, we isolate the maxima f_c of the synchrotron emission, shown with circle markers in Figure 1(B), and construct the spectra of the optically thin emission above f_c , as displayed in Figure 4(C). We follow the evolution of this spectrum over a 72 minute period from 06:00 to 07:12 UT, up until the shock arrives at the observer. Between 06:00 UT and 07:00 UT, α remains constant at approximately 3 ($\delta \sim 7$), which is steeper than the $\delta \sim 4.18$ measured in situ. This discrepancy may arise from large uncertainties in the δ estimated from the data in Figure 4(B). Alternatively, it could indicate that the emission is produced by electrons in the steeper part of the electron distribution, such that f_c corresponds to $\gamma_{\min} > 4$ or $E_e \sim 2$ MeV, where the power law breaks in Figure 4(B). After 07:00 UT, as the shock approaches the observer and f_c approaches f_{pe} , γ_{\min} increases, further steepening α to approximately 5 ($\delta \sim 11$). Between 07:10 UT and 07:12 UT, just before the shock arrives and when the observer is within the emitting region, $\alpha \gtrsim 8$ ($\delta \gtrsim 17$). Similar to S1, this may be a result of the high-frequency exponential synchrotron cut off at γ_{\max} .

Unlike S1, we can directly compare DSA predictions with observations, as the power law extends up to $\gamma \sim 5$, the energy range where electrons are affected by the DSA process. DSA predicts $\delta = 2$, which differs from the observed power-law exponent of $\delta \sim 2.7$, suggesting the presence of additional factors that reduce DSA efficiency. Regarding anisotropy, both HET-A and HET-B detect similar intensities and energies up to ~ 6.7 MeV ($\gamma_{\max} \sim 13$). This indicates that the electrons are isotropic, likely due to the presence of a well-developed foreshock that enables efficient DSA. A final important observation from Figure 4(B) is the order-of-magnitude higher intensity of the entire population of electrons, from subrelativistic to relativistic, compared to what was estimated for S1 in Figure 3(B).

3. Discussion

In this study, we present the first-ever in situ observations of shocks that produced an accelerated power-law distribution of electrons with $\gamma \gg 1$ capable of emitting synchrotron radiation. Unlike the previous remote-sensing study by T. S. Bastian (2007), we experimentally verified the properties of synchrotron emission and the conditions under which it is generated. This was made possible by the unique trajectory of the PSP, which, for the first time, allowed us to study the strongest and fastest IP shocks near their origin at the Sun. Our detailed analysis of both the relativistic electron distribution and the characteristics of the synchrotron radiation led to several key findings, summarized below.

We first demonstrated that the observed radiation characteristics, including spectral morphology and brightness temperature, align with theoretical predictions. For S1, we measured circular polarization in the x -mode, consistent with plasma theory, and found further agreement in the relationship between circular polarization and the γ of the emitting electrons. However, both S1 and S2 exhibited significant deviations from the expected maximum polarization. The theoretical maximum polarization, $\Pi = \frac{3\delta + 3}{3\delta + 7}$, using δ values from S1 and S2, yields $\Pi \sim 80\%$. Notably, emission from S2 was completely depolarized, suggesting that in strongly coupled plasma with multiscale inhomogeneities (both parallel and perpendicular to **B**), such as those found in the solar wind or interstellar medium, the emitted EM wave characteristics may be lost near

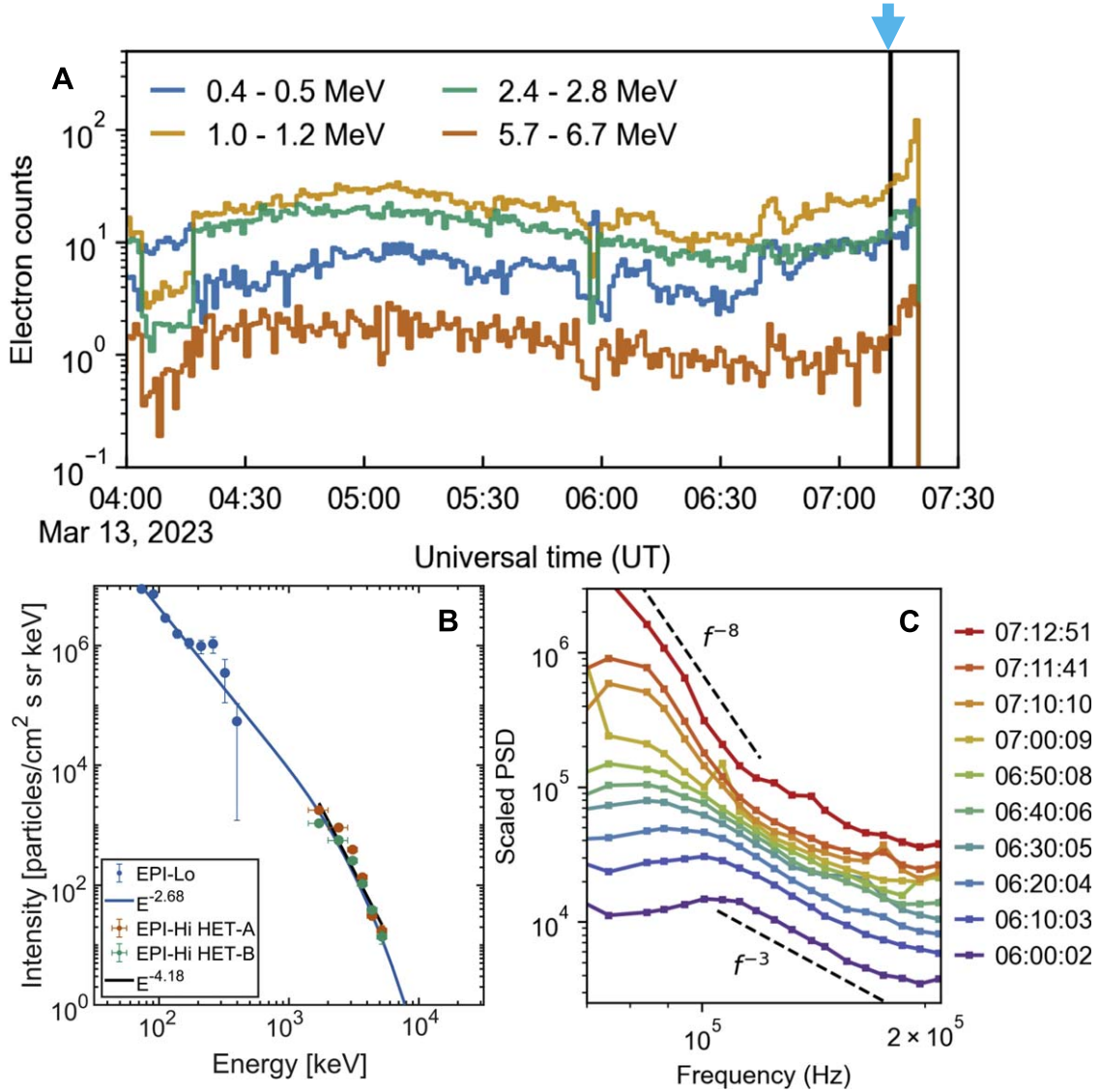


Figure 4. Characteristics of the synchrotron emission from S2 and the corresponding electron distribution. Panel (A) presents the time evolution of the electron intensity in units of counts s^{-1} observed between 04:00 UT and 07:30 UT. The arrival of the shock at PSP is marked by the vertical black line at 07:13 UT and the blue arrow on top. Panel (B) shows the 10 minute averaged electron energy distribution between 07:03 and 07:13 UT in units of particles $cm^{-2} s^{-1} sr^{-1} keV^{-1}$. The different detectors of IS \odot IS used to construct the electron spectrum are annotated with colored markers. The approximate power-law fits and the exponents are also shown in the legend. Panel (C) shows the intensity–frequency profiles at distinct times leading up to the shock arrival, and approximate power-law fits to the optically thin regime are shown.

the emission region. This result is consistent with recent X-ray polarimetric studies of SNRs (J. Vink et al. 2022). These studies show only a small degree of polarization due to a mixture of tangential magnetic field alignment near the shock front and a radially aligned magnetic field structure further from it (A. M. Bykov et al. 2020).

Second, both shocks exhibited similar power-law exponents ($\delta \sim 2.7$ – 2.9) in the low-energy regime before breaking or transitioning to an exponential cutoff. S1 showed partial agreement with DSA predictions for $r_{gas} \sim 2.5$, yielding $\delta \sim 3$. However, because electrons with $\gamma \gtrsim 2$ are required to participate in DSA, and the power law did not extend beyond $\gamma \sim 2$ for S1, it is unclear if DSA was fully active or efficient. Additionally, we observed significant anisotropy, likely due to minimal pitch angle scattering, which suggests that DSA was inefficient. For S2, we found $\delta \sim 2.7$, steeper than the DSA prediction of $\delta = 2$ for $r_{gas} \sim 4$. Despite this, the power law

extended up to $\gamma \sim 5$ before breaking. The electron distribution in S2 was isotropic, a hallmark of efficient DSA.

Lastly, our analysis of the in situ relativistic electron distributions revealed that a quasi-parallel shock like S2 is far more efficient at accelerating electrons than a quasi-perpendicular shock like S1. Electron intensities near the shock where synchrotron emission was generated were an order of magnitude higher for S2 than for S1, resulting in much stronger synchrotron radiation from S2. A plausible explanation is that in quasi-perpendicular shocks, adiabatic acceleration mechanisms likely dominate, resulting in low efficiency for producing relativistic particles (e.g., I. C. Jebaraj et al. 2023b). This suggests that additional mechanisms are required for producing larger populations of relativistic electrons. If DSA were the additional mechanism, its efficiency would be limited by the growth of ion-scale waves through ion-streaming instabilities, a process that is highly inefficient in quasi-

perpendicular shocks like S1 (G. P. Zank & T. K. Gaisser 1992). In contrast, I. C. Jebaraj et al. (2024) found that S2 can locally provide quasi-perpendicular conditions while supporting the efficient growth of ion-scale waves due to its large-scale quasi-parallel geometry making it an efficient accelerator of relativistic electrons.

The last result also experimentally confirms what was observed in the bilateral SNR SN 1006, where the analysis of remote-sensing observations demonstrates that synchrotron emissions from quasi-parallel SNR shocks were significantly brighter than those from oblique and quasi-perpendicular shocks (e.g., R. Rothenflug et al. 2004; R. Giuffrida et al. 2022). This consistency is expected, as the structure of quasi-parallel shocks aligns with theoretical predictions (M. A. Balikhin et al. 2023). Consequently, the nonthermal radiation resulting from the evolutionary behavior of quasi-parallel SNR and IP shocks is likely similar.

The experimental results presented here are the first of their kind, showing that certain IP shocks are capable of persistently accelerating electrons to relativistic energies—a phenomenon previously considered unlikely. The mechanisms by which these shocks accelerate particles and produce radiation resemble those seen in SNR shocks. While detailed quantification of differences between IP and SNR shocks is beyond the scope of this Letter, our work suggests that efficient acceleration is directly related to the upstream bulk flow energy dissipated at the shock in its rest frame.

Acknowledgments

Author contributions. The study was initiated by I.C.J. and conceptualized together with O.V.A., V.V.K., M.G., M.B., and M.M. The methodologies for data analysis were provided by I.C.J., O.V.A., L.V., M.G., A.V., N.D., and R.V. Data analysis was performed by I.C.J., O.V.A., L.V., and A.V. The results were interpreted by I.C.J., O.V.A., M.G., R.V., M.M., V.V.K., J.P., and M.B. The data were visualized by I.C.J., O.V.A., L.V., and A.V. A.M. prepared the schematic. I.C.J. wrote the manuscript and prepared the final draft with significant revisions from M.G. All authors have read the manuscript and agreed to the presented results. The science operations of PSP are led by N.E.R. The operations of the IS \odot IS instrument suite are led by D.J.M., and the data were processed by C.M.S.C., J.G.M., and A.L. The operation of the FIELDS instrument suite is led by S.D.B. and M.P.

Funding Information

The Parker Solar Probe spacecraft was designed and built and is now operated by the Johns Hopkins Applied Physics Laboratory as part of NASA’s Living with a Star (LWS) program (contract NNN06AA01C). Support from the LWS management and technical team has played a critical role in the success of the Parker Solar Probe mission. The authors express their gratitude to all the instrument teams for their work in processing and publishing the publicly available data from the Parker Solar Probe. The data used in this study are available at the NASA Space Physics Data Facility (SPDF), <https://spdf.gsfc.nasa.gov>. This research was supported by the International Space Science Institute (ISSI) in Bern through ISSI International Team project No. 23-575, “Collisionless Shock as a Self-Regulatory System.” This research was supported through the Visiting Scientist program of the International Space Science

Institute (ISSI) in Bern. I.C.J., L.V., and N.D. are grateful for support by the Research Council of Finland (SHOCKSEE, grant No. 346902) and the European Union’s (EU’s) Horizon 2020 research and innovation program under grant agreement No. 101004159 (SERPENTINE) and No. 101134999 (SOLER). The study reflects only the authors’ view, and the European Commission is not responsible for any use that may be made of the information it contains. O.V.A. was partially supported by NSF grant No. 1914670, NASA’s Living with a Star (LWS) program (contract 80NSSC20K0218), and NASA grant contracts 80NNSC19K0848, 80NSSC22K0433, and 80NSSC22K0522. O.V.A. and V.V.K. were supported by NASA grants 80NSSC20K0697 and 80NSSC21K1770. L.V. acknowledges the financial support of the University of Turku Graduate School. V.V.K. also acknowledges financial support from CNES through grants “Parker Solar Probe” and “Solar Orbiter.” A.K. acknowledges financial support from a NASA NNN06AA01C (PSP EPI-Lo) contract. N.W. acknowledges funding from the Research Foundation—Flanders (FWO—Vlaanderen, fellowship no. 1184319N). E.P. acknowledges support from NASA’s Parker Solar Probe Guest Investigators (PSP-GI; grant No. 80NSSC22K0349) and Living With a Star (LWS; grant No. 80NSSC19K0067) programs. E.K. and J.P. acknowledge the Finnish Center of Excellence in Research of Sustainable Space, Project 352850, for supporting this research. J.P. acknowledges support from the Research Council of Finland (SWATCH, grant No. 343581). The FIELDS experiment was developed and is operated under NASA contract NNN06AA01C.

Appendix A Experimental Details

A.1. FIELDS

Our study primarily utilizes the high-frequency electric field measurements from both the HFR and LFR of the RFS (M. Pulupa et al. 2017). These measurements are made by the FIELDS instrument suite on board the PSP spacecraft (S. D. Bale et al. 2016). RFS includes four electric antennas (V_1 , V_2 , V_3 , and V_4) and measures over a wide frequency range, spanning from 20 MHz to 1 kHz at a 3.5 s cadence during close encounters. The frequency resolutions is 4% at any given time over 64 channels in LFR and 64 in HFR.

Additionally, PSP measures the full EM fields for which, the coordinate system used throughout the manuscript is the inertial radial–tangential–normal system, where the radial component R is oriented along the Sun–spacecraft line, the transverse component T is defined to be orthogonal to the rotational axis of the Sun and the radial component, i.e., $T = \Omega_{\odot} \times R$, while the normal component N completes the orthogonal right-handed triad and, in this case, is aligned with the normal of the ecliptic plane. The electric field measurements are made using the electric fields instrument consisting of two pairs of dipole electric field antennas oriented in the TN plane and extending beyond the PSP heat shield and a fifth antenna located behind the heat shield on the instrument boom; the location of antenna V_5 in the wake of PSP means the R component is susceptible to detrimental interference by the wake electric field and cannot be reliably interpreted (S. D. Bale et al. 2016). Two three-component flux-gate magnetometers measure the magnetic field from DC up to 293

vector measurements per second during 2–4 days around close encounter. The latter is used in the present study.

The Time Domain Sampler (TDS) provides high-frequency measurements of waveforms at a rate of about 1.92 million samples s^{-1} . Waveform events captured by TDS consist of 15 ms of the electric (two components) and magnetic (one component) field measurements (S. D. Bale et al. 2016). TDS recorded 66 events on 2022 September 5 between 16:00 and 17:30 UT and 66 events on 2023 March 13 between 04:00 and 07:30 UT. These events were used to compliment the HFR/LFR data.

A.2. IS \odot IS

To analyze the energetic electron spectra close to the shock, we used the IS \odot IS instrument suite (D. J. McComas et al. 2016). It measures energetic particles from ~ 20 keV to over 100 MeV nuc^{-1} with two EPIs, EPI-Lo (M. E. Hill et al. 2017) and EPI-Hi (M. E. Wiedenbeck et al. 2017). EPI-Lo measures energetic electrons primarily through the “ChanE” data product, which utilizes a single silicon solid-state detector (SSD) for the energy measurement and a secondary SSD in anticoincidence with the front SSD to reject penetrating electrons. The HET within EPI-Hi provides measurements of higher-energy electrons with minimal contamination from incident ions. HET is a double-ended dE/dx versus residual energy telescope with one aperture (HET-A) pointed toward the Sun along a nominal Parker spiral and HET-B pointing the opposite direction. For both EPI-Lo and EPI-Hi/HET, the measured electron spectra were unfolded using the response matrix technique to account for the contribution of higher-energy electrons being measured in a lower-energy bin. Full details of the Monte Carlo simulations utilized to construct these response matrices are provided in J. G. Mitchell (2022)

and A. Labrador et al. (2023). While EPI-Hi/HET electron measurements are essentially unaffected by ion contamination, EPI-Lo ChanE can have substantial contamination from high-energy ions when there is a significant Solar Energetic Particle (SEP) ion foreground (J. G. Mitchell et al. 2021). The EPI-Lo response matrix factors in contamination from high-energy ions and reliably separates them from the electron signals (J. G. Mitchell 2022). As such, only the filled markers in Figure 3 should be interpreted as being produced by electrons.

During normal operation, all detector segments in EPI-Hi/HET are sensitive to protons, alphas, electrons, and heavier ions. In periods of high energetic particle intensity, the EPI-Hi instruments employ automated “dynamic threshold” states that raise the trigger thresholds of some detector segments such that they are sensitive only to $Z \geq 6$ ions. This lowers the effective geometry factor of the instrument for protons, alphas, and electrons and keeps the instrument livetime from dropping to low levels while also preserving the ability to measure heavy ions during large events. In the case of the most restrictive dynamic threshold state, HET electron sensitivity is reduced in the energy range of ~ 2 –5 MeV.

Appendix B Transverse EM Wave Properties

Figure 5 displays a waveform captured by the FIELDS/TDS on 2023 March 13. The electric field measurements depicted in panels (a) and (b) reveal the presence of a wave with a frequency of approximately 60 kHz, which aligns with the synchrotron emission illustrated in Figure 1. Magnetic field measurements in panel (c) exhibit only 150 kHz noise, indicating that the magnetic aspect of the wave is too faint for detection by the Search Coil Magnetometer.

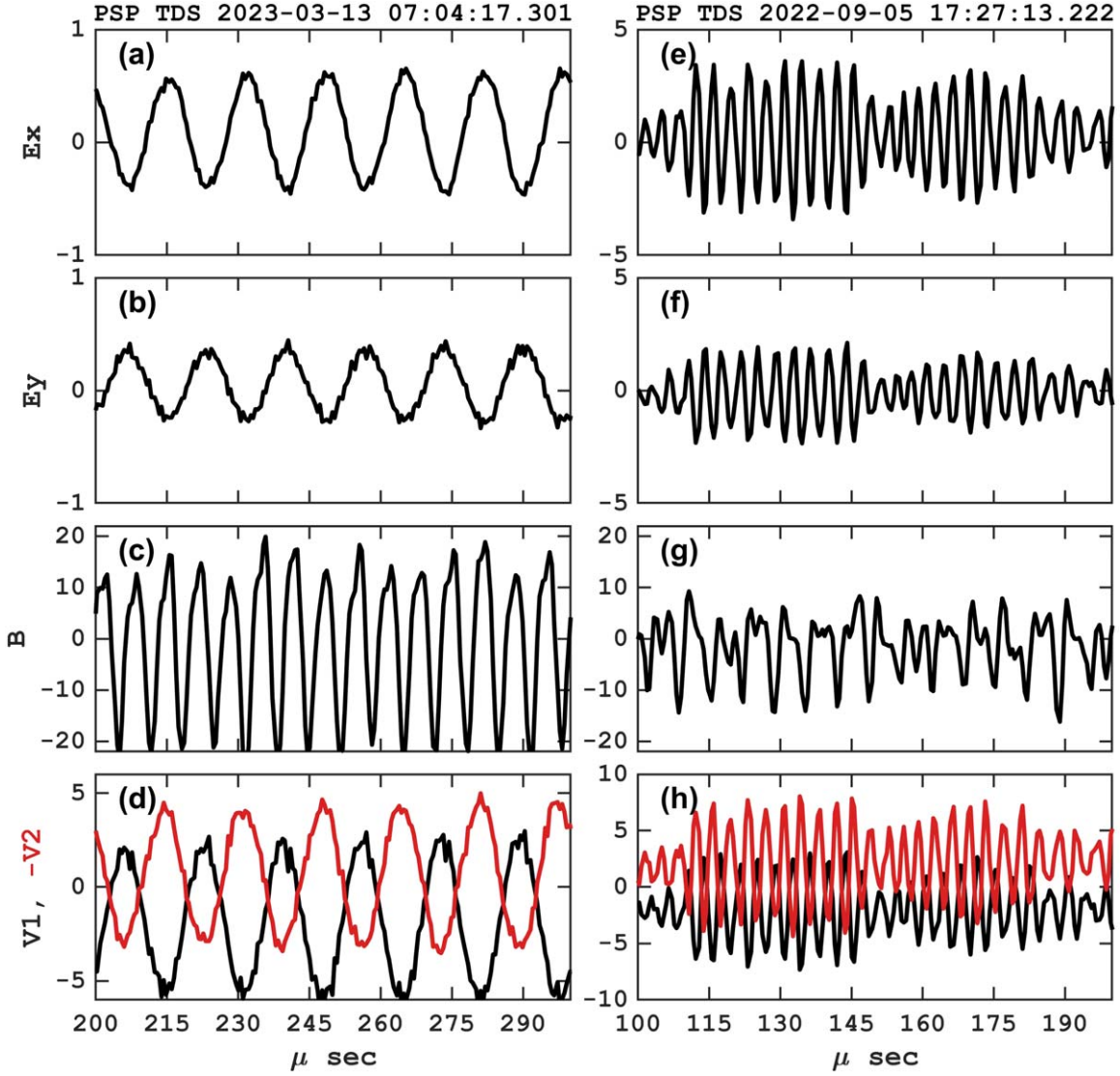


Figure 5. The potential waveforms recorded by TDS on 2023 March 13, 07:04:17.301. (a) and (b) Two components of the electric field. (c) The magnetic field. (d) The potential recorded on antenna 1 (black) and 2 (red). Panels (e)–(h): waveforms recorded by FIELDS/TDS on 2022 September 5, 17:27:13.222.

For further insights into the wave characteristics, we have performed processing of the plasma potential recorded by V_1 and V_2 in panel (d). Notably, the absence of a phase difference in the time profiles allows for estimations of the lower limits of the wavelength and phase velocity of the recorded wave. Given the separation distance between the antennas, denoted as $L \sim 4$ m, and the time step $\Delta t \sim 0.5 \times 10^{-6}$ s, the wavelength is estimated to exceed $L/(f\Delta t) \sim 133$ m. Consequently, the resulting phase velocity greatly exceeds $\sim 7.8 \times 10^3$ km s $^{-1}$. These derived values surpass those anticipated for any electrostatic plasma wave under the prevailing plasma conditions. Analysis of the waveforms recorded on 2022 September 5 gave similar results. Example of waves with a frequency of approximately 420 kHz (consistent with the synchrotron emission illustrated Figure 1) are shown in panels (e)–(h).

Appendix C Estimating Brightness Temperature

The brightness temperatures of synchrotron sources have an upper limit at low frequencies due to synchrotron self-absorption, limiting the maximum brightness temperature to

that of the kinetic temperature of the emitting electrons. For a nonthermal source where the electron energy distribution follows a power law, the brightness temperature cannot exceed the effective temperature of the relativistic electrons responsible for the emission at a given frequency.

At sufficiently low frequencies, the brightness temperature T_B approaches the effective electron temperature T_e , calculated as

$$T_e \sim \left(\frac{2\pi m_e c f}{eB} \right)^{1/2} \frac{2m_e c^2}{3k_B}. \quad (\text{C1})$$

The brightness temperature in the Rayleigh–Jeans limit is defined as

$$T_B = \frac{I_f c^2}{2k_B f^2}. \quad (\text{C2})$$

For an optically thick synchrotron source, T_B cannot exceed T_e , and the flux density S relates to T_B through

$$S = 2k_B T_B f^2 \Omega / c^2, \quad (\text{C3})$$

where Ω is the solid angle subtended by the source. In order to estimate the brightness temperature of the radiation, this solid angle needs to be estimated. The solid angle for distant astrophysical sources is approximated to be $\Omega = \pi\theta^2$, but for sources much closer, this approximation falls apart. For large angles subtended by the source, $\Omega = 2\pi(1 - \cos\theta)$ (S. Chandrasekhar 1960). Here, we estimate $\theta = \arctan(s/D)$ by taking the distance between the shock at $r \sim V_{\text{shock}}\Delta t$ and the observer at r_{sc} as $D = r_{\text{sc}} - r$ and the source width as $s \sim r$. For S1, we assume $V_{\text{shock}} = 1800 \text{ km s}^{-1}$, and for S2, $V_{\text{shock}} = 2500 \text{ km s}^{-1}$ based on simple transit time estimations.

T_B of a synchrotron source that absorbs its own radiation is restricted by inverse Compton scattering, with a theoretical maximum around 10^{12} K , as noted by K. I. Kellermann & I. I. K. Pauliny-Toth (1969). This limit is given by the ratio of inverse Compton to synchrotron cooling and depends primarily on (dfT_B^5) , being highly sensitive to brightness temperature. Here

$$d = \frac{1}{1 - \alpha} \left(\frac{f_{\text{max}}}{f_c} \right)^{1 - \alpha}, \quad (\text{C4})$$

where α is the spectral index of the synchrotron spectrum, f_{max} is the maximum frequency of the synchrotron emission, and f_c is the turnover frequency below which self-absorption is active. d is a dimensionless parameter that is of order 10 for astronomical sources and becomes critical for determining the inverse Compton scattering limit. For typical values of d and f , the brightness temperature limit to prevent the Compton catastrophe is

$$T_B < 1.5 \times 10^{12} \left(\frac{f}{10^9 \text{ Hz}} \right)^{-1/5} \left(\frac{d}{10} \right)^{-1/5} \text{ K}. \quad (\text{C5})$$

It should be noted that the 10^{12} K limit is given for 1 GHz and for d of order 10, and both f and d scale weakly as $f^{-1/5}$ and $d^{-1/5}$. Given that the frequency at which the synchrotron radiation is observed is ~ 4 orders of magnitude smaller, the limit becomes $\approx 10^{13} \text{ K}$.

Assessing the T_B for Syn-1, Syn-2, and Syn-3 in Figure 6(A), we find that Syn-1 maintains a nearly constant T_B , while the T_B of Syn-2 and Syn-3 increase rapidly prior to shock arrival at 17:27 UT. However, this increase does not exceed the inverse Compton scattering limit of $1.3 \times 10^{13} \text{ K}$, with $f = 400 \text{ kHz}$, and for $\alpha = 3$. Figure 6(B) shows the brightness temperature T_B of the emission, which rises exponentially as the shock nears the spacecraft. The T_B even exceeds the inverse Compton limit of $1.7 \times 10^{13} \text{ K}$ at 07:10, suggesting that $\Omega = 2\pi$, at which point the estimation of T_B becomes unreliable. This indicates that at 07:10 UT, the spacecraft should have been in the region where the electrons emitting synchrotron radiation were being accelerated. This is in line with the conclusions of G. A. Dulk & K. A. Marsh (1982), who find that the T_B of the signal at a specific frequency will be strong only under two conditions. The first is the presence of a substantial population of nonthermal electrons along the line of sight, leading to a high optical depth. Second, the magnetic field is either relatively weak (which necessitates higher harmonics and, therefore, more energetic electrons) or aligned at a small angle to the line of sight, where only high-energy electrons contribute significantly to the emission.

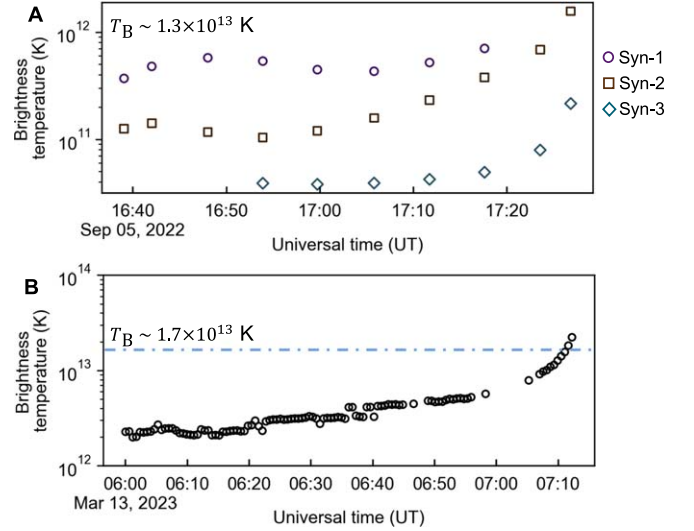


Figure 6. The brightness temperatures (T_B) of the synchrotron emission for S1 and S2 are shown in panels (A) and (B). The inverse Compton scattering limit is explicitly stated in both panels and also represented by the blue dotted-dashed in panel (B).

The limit is widely accepted, and it is important to distinguish synchrotron radiation, which is incoherent, from coherent plasma emissions. The defining characteristic of coherent emissions is their very high intensities (S. Suzuki & G. A. Dulk 1985; V. Krasnoselskikh et al. 2019), which in T_B units greatly exceed 10^{12} K and can reach 10^{18} K (P. Saint-Hilaire et al. 2012). This suggests that coherent emissions have far greater T_B than what is allowed for a hypothetical blackbody radiation of the emitting electrons. Estimating and analyzing the T_B can help in the identification of the emission mechanism. When T_B exceeds the limits found here, it rules out synchrotron radiation as the primary emission process.

Appendix D Polarization

A monochromatic EM wave of the frequency ω is observed at a receiver by measuring the electric field \mathbf{E} that lies in the plane perpendicular to the line of sight, i.e., the direction of propagation. This electric field is conveniently represented as $\mathbf{E} = \text{Re}(\mathbf{E}\hat{\mathbf{e}}e^{-i\omega t})$. The real amplitude E determines the intensity, while the complex unit polarization vector $\hat{\mathbf{e}}$ fully determines the axes of the polarization ellipse and the direction of the electric vector rotation for the completely polarized wave. If the emission comes from many sources, the receiver measures a superposition of many waves,

$$\mathbf{E} = \sum_i \text{Re}(E_i \hat{\mathbf{e}}_i e^{-i\omega t}), \quad (\text{D1})$$

where the summation is over the ensemble of the emitters. Since all E_i and $\hat{\mathbf{e}}_i$ may be different and independent, it is not possible to describe the emission with a single polarization axis. Instead, the Stokes parameters are widely used (S. Chandrasekhar 1947; G. B. Rybicki & A. P. Lightman 1979). These parameters are the differences of average intensities projected onto several sets of unit vectors. Let the plane of the electric field be the $x - y$ plane. Consider the following pairs of unit vectors: (a) $\hat{\mathbf{e}}_x = \hat{x}$, $\hat{\mathbf{e}}_y = \hat{y}$; (b) $\hat{\mathbf{e}}_a = (\hat{x} + \hat{y})/\sqrt{2}$, $\hat{\mathbf{e}}_b = (\hat{x} - \hat{y})/\sqrt{2}$; and (c) $\hat{\mathbf{e}}_R = (\hat{x} + i\hat{y})/\sqrt{2}$, $\hat{\mathbf{e}}_L = (\hat{x} - i\hat{y})/\sqrt{2}$. Then the Stokes

parameters are defined as follows:

$$I = \langle |\mathbf{E} \cdot \hat{\mathbf{e}}_x|^2 \rangle + \langle |\mathbf{E} \cdot \hat{\mathbf{e}}_y|^2 \rangle, \quad (\text{D2})$$

$$Q = \langle |\mathbf{E} \cdot \hat{\mathbf{e}}_x|^2 \rangle - \langle |\mathbf{E} \cdot \hat{\mathbf{e}}_y|^2 \rangle, \quad (\text{D3})$$


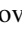




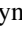
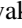





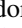




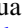






$$U = \langle |\mathbf{E} \cdot \hat{\mathbf{e}}_a|^2 \rangle - \langle |\mathbf{E} \cdot \hat{\mathbf{e}}_b|^2 \rangle, \quad (\text{D4})$$

$$V = \langle |\mathbf{E} \cdot \hat{\mathbf{e}}_R|^2 \rangle - \langle |\mathbf{E} \cdot \hat{\mathbf{e}}_L|^2 \rangle, \quad (\text{D5})$$

where $\langle \dots \rangle$ means ensemble averaging, which corresponds to the averaging of the observations over the time much larger than $1/\omega$. Accordingly, the linear polarization degree is $\Pi_{\text{lin}} = \sqrt{Q^2 + U^2}/I$, the circular polarization degree is $\Pi_{\text{cir}} = V/I$, and the total polarization degree is $\Pi_{\text{tot}} = \sqrt{Q^2 + U^2 + V^2}/I$.

This final expression, Π_{tot} , is important since it is used in observational astronomy to determine the characteristics of the cosmic object and the medium in which it is situated (A. M. Bykov et al. 2012). In radio astronomy, Stokes parameters are often calculated by converting incident electric fields into voltages, where the detection process yields power proportional to the square of these voltages. The raw data, initially in arbitrary units, is calibrated to brightness temperature (K) or flux density ($\text{W m}^{-2} \text{Hz}^{-1}$), with a constant factor accounting for intensity calibration. The exact details of how PSP data are calibrated and the polarization is estimated can be found in M. Pulupa et al. (2017).

ORCID iDs

I. C. Jebaraj  <https://orcid.org/0000-0002-0606-7172>
 O. V. Agapitov  <https://orcid.org/0000-0001-6427-1596>
 M. Gedalin  <https://orcid.org/0000-0003-1236-4787>
 L. Vuorinen  <https://orcid.org/0000-0002-2238-109X>
 M. Miceli  <https://orcid.org/0000-0003-0876-8391>
 C. M. S. Cohen  <https://orcid.org/0000-0002-0978-8127>
 A. Voshchepynets  <https://orcid.org/0000-0001-8307-781X>
 A. Kouloumvakos  <https://orcid.org/0000-0001-6589-4509>
 N. Dresing  <https://orcid.org/0000-0003-3903-4649>
 A. Marmyleva  <https://orcid.org/0000-0003-1175-7124>
 V. Krasnoselskikh  <https://orcid.org/0000-0002-6809-6219>
 M. Balikhin  <https://orcid.org/0000-0002-8110-5626>
 J. G. Mitchell  <https://orcid.org/0000-0003-4501-5452>
 A. W. Labrador  <https://orcid.org/0000-0001-9178-5349>
 N. Wijsen  <https://orcid.org/0000-0001-6344-6956>
 E. Palmerio  <https://orcid.org/0000-0001-6590-3479>
 L. Colombari  <https://orcid.org/0000-0001-6016-7548>
 J. Pomoell  <https://orcid.org/0000-0003-1175-7124>
 E. K. J. Kilpua  <https://orcid.org/0000-0002-4489-8073>
 M. Pulupa  <https://orcid.org/0000-0002-1573-7457>
 F. S. Mozer  <https://orcid.org/0000-0002-2011-8140>
 N. E. Raouafi  <https://orcid.org/0000-0003-2409-3742>
 D. J. McComas  <https://orcid.org/0000-0001-6160-1158>
 S. D. Bale  <https://orcid.org/0000-0002-1989-3596>
 R. Vainio  <https://orcid.org/0000-0002-3298-2067>

References

Agapitov, O. V., Krasnoselskikh, V., Balikhin, M., et al. 2023, *ApJ*, 952, 154
 Axford, W. I., Leer, E., & Skadron, G. 1977, *ICRC (Plovdiv)*, 11, 132
 Bale, S. D., Goetz, K., Harvey, P. R., et al. 2016, *SSRv*, 204, 49
 Balikhin, M., Gedalin, M., & Petrukovich, A. 1993, *PhRvL*, 70, 1259
 Balikhin, M., Krasnosel'skikh, V. V., Woolliscroft, L. J. C., & Gedalin, M. 1998, *JGR*, 103, 2029

Balikhin, M. A., Gedalin, M., Walker, S. N., Agapitov, O. V., & Zhang, T. 2023, *ApJ*, 959, 130
 Balikhin, M. A., Krasnosel'skikh, V. V., & Woolliscroft, L. J. C. 1989, *AdSpR*, 9, 203
 Bastian, T. S. 2007, *ApJ*, 665, 805
 Bell, A. R. 1978, *MNRAS*, 182, 147
 Blandford, R. D., & Ostriker, J. P. 1978, *ApJL*, 221, L29
 Born, M., & Wolf, E. 1964, *Principles of Optics Electromagnetic Theory of Propagation, Interference and Diffraction of Light* (2nd ed.; London: MacMillan)
 Bykov, A. M. 2004, *AdSpR*, 33, 366
 Bykov, A. M., Ellison, D. C., Marcowith, A., & Osipov, S. M. 2019, in *Supernovae*, ed. A. Bykov et al., Vol. 68 (Berlin: Springer), 419
 Bykov, A. M., Ellison, D. C., & Renaud, M. 2012, *SSRv*, 166, 71
 Bykov, A. M., Uvarov, Y. A., Slane, P., & Ellison, D. C. 2020, *ApJ*, 899, 142
 Cairns, I. H., Knock, S. A., Robinson, P. A., & Kuncic, Z. 2003, *SSRv*, 107, 27
 Chandrasekhar, S. 1947, *BAMaS*, 53, 641
 Chandrasekhar, S. 1960, *Radiative Transfer* (New York: Dover)
 Drury, L. O. 1983, *RPPh*, 46, 973
 Dulk, G. A., & Marsh, K. A. 1982, *ApJ*, 259, 350
 Fox, N. J., Velli, M. C., Bale, S. D., et al. 2016, *SSRv*, 204, 7
 Galeev, A. A. 1976, in *Physics of Solar Planetary Environments*, Proc. of the Int. Symp. on Solar-Terrestrial Physics, ed. D. J. Williams (Washington, DC: AGU), 464
 Galeev, A. A., & Krasnoselskikh, V. V. 1979, *SvAL*, 5, 257
 Gedalin, M. 2020, *ApJ*, 895, 59
 Gedalin, M., Gedalin, K., Balikhin, M., Krasnoselskikh, V., & Woolliscroft, L. J. C. 1995, *JGR*, 100, 19911
 Ginzburg, V. L. 1979, *Theoretical Physics and Astrophysics* (Oxford: Pergamon)
 Ginzburg, V. L., & Syrovatskii, S. I. 1964, *The Origin of Cosmic Rays* (Amsterdam: Elsevier)
 Ginzburg, V. L., & Syrovatskii, S. I. 1969, *ARA&A*, 7, 375
 Giuffrida, R., Miceli, M., Caprioli, D., et al. 2022, *NatCo*, 13, 5098
 Green, D. A. 2019, *JApA*, 40, 36
 Helder, E. A., Vink, J., Bassa, C. G., et al. 2009, *Sci*, 325, 719
 Hill, M. E., Mitchell, D. G., Andrews, G. B., et al. 2017, *JGRA*, 122, 1513
 Jebaraj, I. C., Agapitov, O., Krasnoselskikh, V., et al. 2024, *ApJL*, 968, L8
 Jebaraj, I. C., Dresing, N., Krasnoselskikh, V., et al. 2023a, *A&A*, 680, L7
 Jebaraj, I. C., Krasnoselskikh, V., Pulupa, M., Magdalenic, J., & Bale, S. D. 2023b, *ApJL*, 955, L20
 Jebaraj, I. C., Magdalenic, J., Podladchikova, T., et al. 2020, *A&A*, 639, A56
 Kaplan, S. A., & Tsytoich, V. N. 1969, *SvPhU*, 12, 42
 Katou, T., & Amano, T. 2019, *ApJ*, 874, 119
 Kellermann, K. I., & Pauliny-Toth, I. I. K. 1969, *ApJL*, 155, L71
 Kennel, C. F., Edmiston, J. P., & Hada, T. 1985, *GMS*, 34, 1
 Krasnoselskikh, V., Balikhin, M., Walker, S. N., et al. 2013, *SSRv*, 178, 535
 Krasnoselskikh, V., Voshchepynets, A., & Maksimovic, M. 2019, *ApJ*, 879, 51
 Krymskii, G. F. 1977, *DoSSR*, 234, 1306
 Labrador, A., Mitchell, G., Christian, E., et al. 2023, *ICRC (Nagoya)*, 444, 1315
 Lembege, B., Giacalone, J., Scholer, M., et al. 2004, *SSRv*, 110, 161
 Liu, M., Issautier, K., Moncuquet, M., et al. 2023, *A&A*, 674, A49
 Lobzin, V. V., Krasnoselskikh, V. V., Schwartz, S. J., et al. 2005, *GeoRL*, 32, L18101
 Longair, M. S. 1992, *High Energy Astrophysics. Vol.1: Particles, Photons and their Detection* (Cambridge: Cambridge Univ. Press)
 Malkov, M. A., & Drury, L. O. 2001, *RPPh*, 64, 429
 McComas, D. J., Alexander, N., Angold, N., et al. 2016, *SSRv*, 204, 187
 Melrose, D. B. 1971, *Ap&SS*, 12, 172
 Miceli, M. 2023, *PPCF*, 65, 034003
 Mitchell, J. G. 2022, PhD thesis, George Washington Univ.
 Mitchell, J. G., De Nolfo, G. A., Hill, M. E., et al. 2021, *ApJ*, 919, 119
 Nindos, A. 2020, *FrASS*, 7, 57
 Papadopoulos, K., & Freund, H. P. 1979, *SSRv*, 24, 511
 Pohjolainen, S., Allawi, H., & Valtonen, E. 2013, *A&A*, 558, A7
 Pulupa, M., Bale, S. D., Bonnell, J. W., et al. 2017, *JGRA*, 122, 2836
 Ramaty, R. 1969, *ApJ*, 158, 753
 Riquelme, M. A., & Spitkovsky, A. 2011, *ApJ*, 733, 63
 Romeo, O. M., Braga, C. R., Badman, S. T., et al. 2023, *ApJ*, 954, 168
 Rothenflug, R., Ballet, J., Dubner, G., et al. 2004, *A&A*, 425, 121
 Rybicki, G. B., & Lightman, A. P. 1979, *Radiative Processes in Astrophysics* (New York: Wiley)
 Sagdeev, R. Z. 1966, *RvPP*, 4, 23
 Saint-Hilaire, P., Vilmer, N., & Kerdran, A. 2012, *ApJ*, 762, 60
 Schwinger, J. 1949, *PhRv*, 75, 1912

- Sitenko, A. G., & Kirochkin, Y. A. 1966, [SvPhU](#), **9**, 430
- Suzuki, S., & Dulk, G. A. 1985, in *Solar Radiophysics: Studies of Emission from the Sun at Meter Wavelengths*, ed. D. J. McLean & N. R. Labrum (Cambridge: Cambridge Univ. Press), 289
- Talebpour Sheshvan, N., Dresing, N., Vainio, R., Afanasiev, A., & Morosan, D. E. 2023, [A&A](#), **674**, A133
- Terasawa, T. 2003, [PThPS](#), **151**, 95
- Trotta, D., Larosa, A., Nicolaou, G., et al. 2024, [ApJ](#), **962**, 147
- Vainio, R. 2003, [A&A](#), **406**, 735
- Vainio, R., & Schlickeiser, R. 1999, [A&A](#), **343**, 303
- Vink, J. 2020, *Physics and Evolution of Supernova Remnants* (Berlin: Springer)
- Vink, J., Prokhorov, D., Ferrazzoli, R., et al. 2022, [ApJ](#), **938**, 40
- Voshchepynets, A., Krasnoselskikh, V., Artemyev, A., & Volokitin, A. 2015, [ApJ](#), **807**, 38
- Wiedenbeck, M. E., Angold, N. G., Birdwell, B., et al. 2017, [ICRC \(Busan\)](#), **301**, 16
- Zank, G. P., & Gaisser, T. K. (ed.) 1992, in *AIP Conf. Ser. 264, Particle Acceleration in Cosmic Plasmas* (Melville, NY: AIP)
- Zheleznyakov, V. V. 1968, [Ap&SS](#), **2**, 417